

Versatile Tunability of the Metal Insulator Transition in $(\text{TiO}_2)_m/(\text{VO}_2)_m$ Superlattices

Gyula Eres,* Shinbuhm Lee, John Nichols, Changhee Sohn, Jong Mok Ok, Alessandro R. Mazza, Chenze Liu, Gerd Duscher, Ho Nyung Lee, Daniel E. McNally, Xingyu Lu, Milan Radovic,* and Thorsten Schmitt*

In contrast to perovskites that share only common corners of cation-occupied octahedra, binary-oxides in addition share edges and faces increasing the versatility for tuning the properties and functionality of reduced dimensionality systems of strongly correlated oxides. This approach for tuning the electronic structure is based on the ability of X-ray spectroscopy methods to monitor the creation and transformation of occupied and unoccupied electronic states produced by interface coupling and lattice distortions. X-ray diffraction reveals a new range of structural metastability in $(\text{TiO}_2)_m/(\text{VO}_2)_m/\text{TiO}_2(001)$ superlattices with $m = 1, 3, 5, 20, 40$, and electrical transport measurements show metal insulator transition (MIT) behavior typically associated with presence of high oxygen vacancy concentrations. However, X-ray absorption spectroscopy (XAS) at the Ti and V $L_{3,2}$ -edge and resonant inelastic X-ray scattering (RIXS) at the Ti and V L_3 -edge show no excitations characteristic of oxygen vacancy induced valance change in V and negligible intensities in Ti RIXS. The unexpected absence of oxygen vacancy related states in the X-ray spectroscopy data suggests that superlattice fabrication is capable of suppressing oxygen vacancy formation while still affording a wide tunability range of the MIT. Achieving a wide range of MIT tunability while reducing or eliminating oxygen vacancies that are detrimental to electrical properties is highly desirable for technological applications of strongly correlated oxides.

understanding the fundamental physics of strongly correlated behavior underlying the MIT, the tunability range of VO_2 properties is critical for developing novel solid-state devices that can be switched by non-thermal external stimuli.^[4–7] VO_2 has a d^1 configuration that according to conventional electron counting rules corresponds to a paramagnetic metal. The SPT occurs between this high temperature metallic rutile (R) phase and a low temperature insulating monoclinic (M_1) phase. It proceeds by interaction of two structural elements including the formation of V–V dimers between neighboring V atoms and their tilting perpendicular to the rutile c -axis. The V–V dimerization distorts the bonding in adjacent VO_6 oxygen octahedra resulting in a complex interplay between the charge, spin, orbital, and lattice degrees of freedom that produces the instabilities manifested by the MIT.^[8,9] Despite numerous experimental and theoretical studies since its discovery in 1959, no consensus has emerged on the fundamental physics governing the VO_2 MIT mechanism.^[1,2,8,9]

1. Introduction

Vanadium dioxide (VO_2) is an archetypal strongly correlated material that exhibits a metal insulator transition (MIT) concomitant with a structural phase transition (SPT) slightly above room temperature at around 340 K.^[1–3] In addition to

In general, the approach for interpretation of the MIT includes two different starting points.^[10] The dimerization of the V atoms is believed to indicate that the MIT is driven by structural distortions and strong electron-lattice coupling that are the features of Peierls physics.^[11] The second mechanism incorporates strong electron correlations such as Coulomb

Dr. G. Eres, Prof. S. Lee, Dr. J. Nichols, Dr. C. Sohn, Dr. J. M. Ok, Dr. A. R. Mazza, Dr. H. N. Lee
Oak Ridge National Laboratory
Materials Science and Technology Division
Oak Ridge, TN 37831, USA
E-mail: eresg@ornl.gov

 The ORCID identification number(s) for the author(s) of this article can be found under <https://doi.org/10.1002/adfm.202004914>.

© 2020 Oak Ridge National Laboratory. Published by Wiley-VCH GmbH. This is an open access article under the terms of the Creative Commons Attribution License, which permits use, distribution and reproduction in any medium, provided the original work is properly cited.

Prof. S. Lee
Department of Emerging Materials Science
Daegu-Gyeongbuk Institute of Science and Technology
Daegu 42988, Republic of Korea

Dr. C. Liu, Prof. G. Duscher
Department of Materials Science and Engineering
University of Tennessee
Knoxville, TN 37996, USA

Dr. D. E. McNally, Dr. X. Lu, Prof. M. Radovic, Dr. T. Schmitt
Paul Scherrer Institut
Photon Science Division
Villigen PSI CH-5232, Switzerland
E-mail: milan.radovic@psi.ch; thorsten.schmitt@psi.ch

DOI: 10.1002/adfm.202004914

repulsion between the localized V $3d$ orbitals that is characteristic of Mott–Hubbard physics.^[8,12–14] Mounds of experimental data accumulated that under certain conditions appear to favor one or the other mechanism. Recent experiments show that phonon modes, and the stability and the rate of disordering of the V–V dimers across the MIT hold important clues about the mechanism of the phase transition.^[15–17] Based on the most recent experimental data and theoretical calculations the VO₂ MIT is now understood as a cooperative Mott–Peierls transition involving both lattice and electron correlation effects.^[9,17] The overall picture is complicated further by the appearance of an intermediate monoclinic M_2 phase in which half of the V atoms form dimers that do not twist, and the other half form unpaired zigzag chains. It is important to note that strain plays a key role in the occurrence of the M_2 phase, as well as the formation and stability of all other lower-symmetry vanadium oxide phases. The M_2 phase can be stabilized by changing the TiO₂ substrate orientation and tuning the type and level of strain produced by compression or elongation along the c -axis direction.^[17–19] Using non-thermal excitations to induce the MIT provides additional clues for understanding the mechanism of MIT.^[20]

The starting point for understanding the complex landscape of coupling between the structural and the electronic degrees of freedom driving the MIT is the qualitative picture, provided by the molecular orbital (MO) model proposed by Goodenough.^[11] This model uses the orbital configuration and the orbital populations of the V $3d$ energy levels to interpret the electronic structure changes during the VO₂ MIT. In a perfectly octahedral crystal field, the five V $3d$ orbitals are split into lower triply degenerate t_{2g} and upper doubly degenerate e_g sets of orbitals. The reduced symmetry of the tetragonal R field lifts the degeneracy and creates two types of t_{2g} orbitals; the higher energy doubly degenerate π^* orbitals, and the remaining lowest energy $d_{x^2-y^2}$ the so-called $d_{||}$ orbital that hosts the electron.^[11,21] The VO₆ octahedra with shared edges form a one-dimensional (1D) chain by V–V bonds between neighboring V atom $d_{||}$ orbitals. The 1D chain is subject to Peierls transition that stabilizes the system by pairing of the V–V atoms (dimerization) along the c -axis chain with alternating longer and shorter bond lengths. The application of strain increases the V–O apical bond length and reduces the energy split between the π^* and $d_{||}$ orbitals that are both populated in the metallic state. Across the MIT in the insulating state the π^* orbitals shift up in energy by the antiferroelectric distortion that increases the p – d overlap and the dimerization splits the $d_{||}$ orbitals into bonding and anti-bonding orbitals opening a gap of about 0.7 eV.^[11,22] This picture also explains why strain has a weak effect on the orbital population in the insulating state.^[21,23] The orbital configuration picture provides novel approaches for controlling the MIT in VO₂ by employing external perturbation for modifying the orbital occupancy.^[21] The main synthesis approaches for tuning the properties of metal oxides include doping, alloying, and superlattice fabrication.^[24–28]

The fabrication of oxide superlattices has unlocked a potential for the discovery and exploration of emergent electric, magnetic, and multiferroic phenomena.^[27] The most widely studied oxide superlattices have the perovskite structure ABO₃, where the A and B sites can be occupied by many different combinations of metal atoms, resulting in a rich variety of phenomena not available in conventional semiconductors.^[27,29] The high stability of

the perovskite structure that makes it attractive for superlattice fabrication stems from sharing a common oxygen sublattice across the heterostructure interface consisting of a corner connected BO₆ octahedral network. A great deal of practical knowledge has been accumulated about perovskite interfaces and their stability with respect to compositional and structural factors. Recently, a few theoretical calculations appeared proposing to use superlattices for tuning the properties and the electronic structure in binary oxides.^[30–32] Specifically, fabrication of VO₂ superlattices was proposed for tuning the electronic structure to create exotic two dimensional electronic states.^[30,31]

The most intriguing prediction of exotic behavior resulting from quantum confinement in (TiO₂)_{*m*}/(VO₂)_{*m*} superlattices is the formation of two-dimensional electronic states as a function of the VO₂ layer thickness sandwiched between two insulating TiO₂ layers.^[30] The theoretical calculations predict that a semi-Dirac point forms when 3 unit cells (uc) of VO₂ are sandwiched between 5 uc thick TiO₂ layers.^[30] The VO₂/TiO₂ interface is the binary oxide equivalent of the extensively studied d_1/d_0 perovskite system.^[28,33,34] However, unlike perovskites, much less is known about the properties and the stability of binary oxide MO₂ superlattices.^[28,35] In contrast to perovskites, the MO₆ octahedra in binary oxides of MO₂ type are interconnected by both edge and tip sharing that facilitates stronger cation–cation interactions expanding the range of properties.^[35] For example, metallicity of these compounds increases with the increasing fraction of edge sharing when going from Ti⁴⁺ in TiO₂, to Ti³⁺ in Ti₂O₃.^[36,37] The interconnectivity also affects phase stability with multiple metastable phases existing in a narrow energy range.^[37] The composition and the phase stability are critical factors that must be controlled by the growth method making binary oxide superlattice fabrication a formidable challenge.^[28,35] Fabrication of superlattices also requires interface control because oxides are known to have intrinsic thickness related properties that alter interface coupling such as dead-layer effects and critical thickness phenomena.^[38]

The combination of X-ray diffraction (XRD), temperature dependent electrical transport, and X-ray spectroscopic measurements was used to characterize the properties of (TiO₂)_{*m*}/(VO₂)_{*m*} superlattices as a function of growth conditions, temperature and periodicity m . The significant new results of this work are related to the spectroscopic states revealing a delicate balance of oxygen vacancies in the VO₂ and TiO₂ layers of the superlattices. Specifically, the simultaneous presence of oxygen vacancy related Ti³⁺ states combined with the lack of oxygen vacancy related V³⁺ states in spectroscopic data suggest that the dramatic changes of the MIT can occur at very low levels of oxygen vacancy induced V³⁺ states. The X-ray spectroscopy data demonstrate that fabrication of superlattices is a highly versatile method for exploring novel properties and functionalities in reduced dimensionality systems of strongly correlated oxides in general.

2. Results and Discussion

2.1. The Dependence of MIT on Structural and Electrical Properties of Superlattices

The room temperature XRD data for a series of superlattices (TiO₂)_{*m*}/(VO₂)_{*m*}/TiO₂(001) with $m = 1, 3, 5, 20,$ and 40 uc are

contraction of the *c*-axis stabilizes the metallic phase.^[23,40,41] The unexpected opposite thickness dependence of the T_{MIT} indicates that the overall strain that governs the electrical properties of the superlattices accumulates from multiple mechanisms.^[40]

In addition to the changing T_{MIT} the shape of the temperature dependent resistivity curves across the phase boundary can provide important hints about the underlying mechanisms that govern the MIT. The data show that for an equivalent thickness VO_2 thin film the phase transition from the M_1 insulating phase to the R metallic phase occurs at 300 K and is accompanied by an abrupt resistivity change ($\Delta R/R$) of more than three orders of magnitude in agreement with the bulk value and data in the literature.^[39–41,46] Except for the $T3V3$ superlattice, which shows no clear MIT, the superlattices are characterized by decreasing $\Delta R/R$ with increasing VO_2 layer thickness. The data show a progressive suppression of the MIT with increasing superlattice period with the resistivity range $\Delta R/R$ completely vanishing for the $T40V40$ superlattice. Interestingly, $\Delta R/R$ almost fully recovers if the layers are grown in the reverse order, with the VO_2 layer on top without a TiO_2 capping layer designated by $V40T40$. However, note that the $V40T40$ superlattice shows a stepwise MIT, which indicates that the phase transition involves multiple phases that have MIT temperatures overlapping in a narrow temperature range.^[41] In a recent report the incorporation of oxygen vacancies into the VO_2 layer was found to be promoted by the presence of a TiO_2 cap layer.^[48] Note that the data in Figure 2 were obtained keeping the total film thickness fixed, with all superlattices capped with a top TiO_2 layer, except the $V40T40$ superlattice and the VO_2 film that had no TiO_2 cap layer. In this new metastability range that is characterized by the shrinking of the *c*-axis lattice constant with increasing layer thickness, the pure VO_2 is an outlier. The different behavior originates from the presence of the TiO_2 layers that impose additional strain mechanisms that are absent in fully optimized stoichiometric pure VO_2 films.

Since the growth conditions have been kept constant, the period (layer thickness) remains the only variable for the superlattices. Although the $\Delta R/R$ is reduced compared to that in the VO_2 thin film, the T_{MIT} and the overall shape of the MIT are both preserved for the $T5V5$ superlattice in Figure 2. From here the MIT undergoes changes in both directions. In the direction of shorter periods it already vanishes for the $T3V3$ superlattice. The range of changes is wider in the direction of longer periods. These trends in the electrical resistivity data also indicate existence of different strain mechanisms that balance out for the growth of the $T5V5$ member, with degradation of the MIT occurring toward both shorter and longer superlattice periods. Like for the strain, the mechanism governing the MIT is also dominated by chemical expansion. It is different for the short period superlattices from that for the long period superlattices. Both the XRD data and the MIT degradation suggest that the mechanism in short period superlattices is more complex and harder to ascertain. It is related to interface intermixing that causes unintended Ti doping, which is known to produce large strain.^[49] It was reported that Ti interdiffusion into the VO_2 layers during thin film growth was found to cover a surprisingly wide range from 2 to 5 nm.^[45,46] However, interdiffusion of Ti alone is not likely to explain such complete degradation. Based on the lattice constant data obtained in

systematic Ti doping studies the lattice constant in the superlattices up to $m = 5$ corresponds to an average of 10% fraction of Ti. These studies also show that the MIT is robust in solid solution alloys up to 20% fraction of Ti.^[24]

The shape of the MIT indicates that the mechanism in the direction of increasing superlattice periods is dictated by oxygen vacancy incorporation.^[43,44,48] Similar trends have been observed in VO_2 thin films where oxygen vacancy incorporation was controlled by the O_2 background pressure during PLD film growth.^[43] In addition, theoretical modeling in a recent report reveals that a spontaneous driving force exists for directional migration of oxygen vacancies from the TiO_2 into the VO_2 layer.^[48] The driving force is generated by the difference in the oxygen vacancy formation energy in VO_2 and TiO_2 layers. The resulting chemical potential mismatch referred to as oxygen diode effect in nickelate heterostructures provides a unidirectional flow of oxygen vacancies into the VO_2 layers.^[48,50] However, it is remarkable that in contrast to numerous reports of oxygen vacancy dominated MIT,^[43,44,48] the X-ray spectroscopy data suggest that these dramatic changes in the MIT occur at very low levels of oxygen vacancies in VO_2 . Specifically, Ti *L*-edge RIXS shows the presence of Ti^{3+} states related to low concentration of oxygen vacancies in the TiO_2 layers. In contrast, the V *L*-edge RIXS shows no $V 3d^2$ features that would indicate the reduction of the V oxidation state from 4+ to 3+ that is a signature of oxygen vacancy presence.

2.2. Characterization of the Electronic Structure of TiO_2 using XAS and RIXS

The electronic structure of both the TiO_2 and the VO_2 layers and their interlayer coupling at superlattice interfaces was characterized by XAS and RIXS.^[51,52] The XAS spectra were measured using either the surface sensitive total electron yield (TEY), or the bulk sensitive total fluorescence yield (TFY) mode when necessary for avoiding surface charging in the insulating phase. The TEY mode was used only after confirming that the signal was representative of the superlattice stack and not just the topmost layer. The XAS spectra of TiO_2 at the Ti $L_{3,2}$ -edge in Figure 3 consist of four peaks labeled $L_{3-t_{2g}}$, L_{3-e_g} , $L_{2-t_{2g}}$, and L_{2-e_g} .^[53,54] The splitting of the L_{3-e_g} peak into a doublet with asymmetric intensity, clearly identifiable for the 40 uc thick TiO_2 layers in $T40V40$ superlattices, has been used routinely as a fingerprint for differentiating between the two most stable polymorphs of TiO_2 , rutile and anatase. Note that for anatase the intensity ratio of the doublet is reversed because the crystal field symmetry, reflecting the difference in the TiO_6 -octahedral distortion, changes from D_{2h} for rutile to D_{2d} for anatase. For the T_mV_m superlattices the L_{3-e_g} doublet in Figure 3 becomes gradually smeared out with decreasing period m . The splitting is still observable for the $T5V5$, but the peak separation is completely washed out for $T3V3$ superlattices. This progression of the spectral shape change is consistent with increasing distortion of the TiO_6 octahedra with decreasing superlattice period. However, theoretical work shows that the origin of the splitting of the L_{3-e_g} peak is still not well understood and the interpretation remains unresolved. Initially the splitting was attributed to a local effect related to distortion of the TiO_6 octahedra by

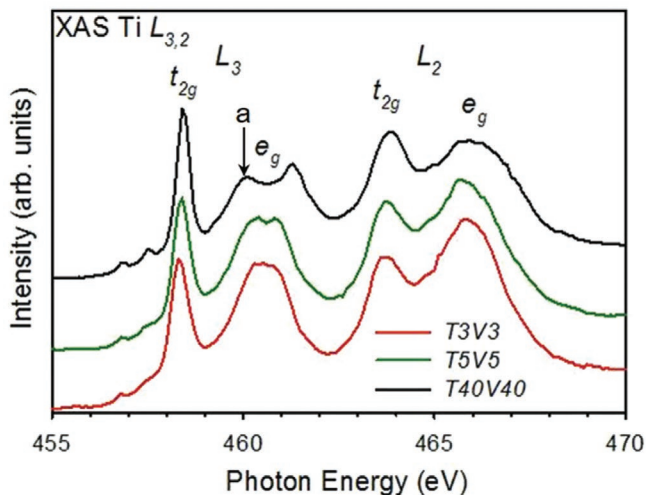


Figure 3. Ti $L_{3,2}$ XAS spectra for $(\text{TiO}_2)_m/(\text{VO}_2)_m$ superlattices as a function of superlattice period m measured at 15 K. The spectra are vertically offset for clarity, $a = 460$ eV indicates the incident photon energy used for RIXS spectra.

a noncubic crystal field.^[55] This interpretation was challenged by arguments that the noncubic field is too weak to produce the distortion needed for the experimentally observed splitting.^[56] A more recent interpretation using a multichannel multiple-scattering approach found that the splitting is a long-range effect reflecting the band structure of TiO_2 on a length scale of about 1 nm.^[53] Based on this interpretation the XAS data can be used to differentiate between the structural effects of the two chemical mechanisms of strain. In the direction of increasing TiO_2 layer thickness the long-range order prevails based on the clear splitting of the L_3 - e_g peak features. In contrast, in the direction of decreasing thickness the splitting of the peaks becomes gradually smeared out, indicating deterioration of long-range order. Using this interpretation of the splitting the spectroscopic evidence and the structural and electrical transport data point to the disruption of long-range order caused by Ti interdiffusion across the interface as the main cause of the deterioration of the MIT with decreasing superlattice period.

Additional information about the details of the electronic structure related to lattice distortion, chemical composition, and the properties of the TiO_2 layers in the superlattices was obtained by RIXS. The 3d transition metal (TM) oxides including TiO_2 and VO_2 are strongly correlated materials. The electronic structure of these systems is characterized by low energy dd and $3d^{n+1}\bar{L}$ charge transfer (CT) excitations, where n represents the 3d occupation number and \bar{L} indicates a ligand hole. The RIXS spectra consist of three main components, the elastic peak at the incident photon energy that is centered at 0 eV on the customarily used energy transfer scale, normal emission spectral components that occur at fixed X-ray emission energy showing dispersion in the energy loss plots, and the most important and revealing inelastic scattering components related to dd and CT excitations.

The $3d^0$ and the $3d^1$ systems are representative of the nominal occupancy of the stoichiometric compounds TiO_2 and VO_2 , respectively. In addition, the presence of oxygen vacancies in the parent compounds changes the occupancy of the

transition metal orbitals reflected by possible Ti^{3+} and V^{3+} states represented by additional $3d^1$ and $3d^2$ components in TiO_2 and VO_2 , respectively, that have distinctly different signatures in the RIXS spectra.^[57–60] RIXS is sensitive to extremely small amounts of Ti^{3+} and V^{3+} despite the presence of majority states Ti^{4+} and V^{4+} , respectively. The Ti L_3 RIXS spectra of TiO_2 layers in **Figure 4** are obtained using incident photon energy of 460 eV, as indicated in **Figure 3**. The 460 eV incident photon energy was selected because it is in the most sensitive energy region for probing the presence of Ti^{3+} states.^[61] The overall Ti $L_{3,2}$ XAS spectrum in the presence of Ti^{3+} represents a linear combination of contributions from both Ti^{3+} and Ti^{4+} states.^[54] Without extra electrons, stoichiometric undoped TiO_2 is a $3d^0$ electronic system, which means that for Ti^{4+} dd transitions are absent.^[62,63] The presence of dd transitions indicates Ti^{3+} states resulting from extra electrons that could have been donated either by VO_2 or created by the formation of oxygen vacancies.^[61] The RIXS spectra in **Figure 4** after normalization by the 8.5 eV CT peak reveal a weak feature near 1.8 eV. This dd peak is produced by excitation into the e_g manifold with the deexcitation step coming from the t_{2g} manifold. It is split for short period superlattices and shifts toward lower energy loss values with increasing superlattice period. The intensity corresponding to the concentration of oxygen vacancies appears to be unaffected by the superlattice period. However, unlike for $\text{LaAlO}_3/\text{SrTiO}_3$ superlattices no additional excitations that could be attributed to localized or delocalized Ti 3d carriers have been observed in this spectral region for the VO_2/TiO_2 superlattices.^[61] We assume that the states associated with the weak dd peak make a negligible contribution to the MIT of the superlattices. This assumption is in agreement with a previous report, which finds that oxygen annealing reduces the intensity but does not eliminate the dd peak.^[64]

In addition to the dd transitions, the Ti L_3 RIXS spectra show low energy excitations in the asymmetric tail of the elastic peak consisting of a sequence of satellite peaks in **Figure 5**.

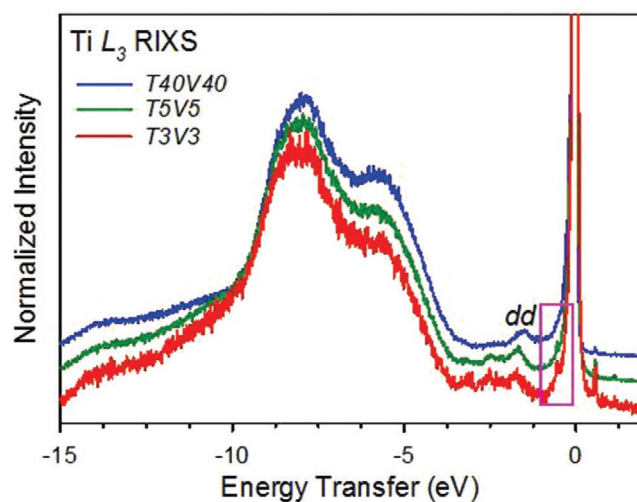


Figure 4. The Ti L_3 RIXS spectra at 15 K compared for three superlattices at incident photon energy $a = 460$ eV from XAS spectra in **Figure 3**. The spectra were normalized by the intensity of the CT peak at 8.5 eV and offset vertically for clarity. The magenta box marks the spectral region of e -ph coupling expanded in **Figure 5**.

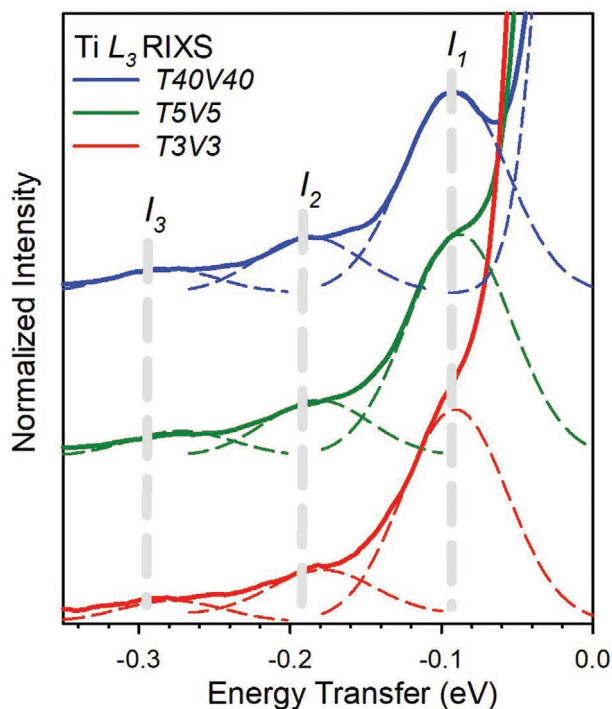


Figure 5. The Ti L_3 RIXS spectra near the elastic peak compared for three superlattices. The peaks I_n ($n = 1-3$) are phonon harmonics signaling sizable electron-phonon coupling in TiO_2 . The spectra were normalized by the intensity of the CT peak at 8.5 eV and offset vertically for clarity.

The intensity of these peaks is exponentially decreasing with a separation of ≈ 90 meV that was attributed to a bond-stretching optical phonon that is producing several harmonics because of the sizable electron-phonon (e -ph) coupling in bulk anatase TiO_2 crystals.^[64] Importantly, our results are the first observation of e -ph coupling in a thin film of the rutile polymorph. The sharpness of the satellite peaks increases with TiO_2 layer thickness. While the peaks appear only as weak undulations for the T3V3 superlattice, they are distinguishable even without subtraction of the elastic peak in T5V5 superlattices and become sharp and clearly separate in a series of peaks I_n ($n = 1-3$) in T40V40 superlattices. The ratio of the one and two-phonon loss peak intensities I_2/I_1 directly reflects the e -ph coupling interaction, and it can be used for estimating the value of the e -ph coupling constant that governs the electrical properties of TiO_2 in the superlattices.^[65] Using the values $I_2/I_1 = 0.28$, 0.23, and 0.21 from the Gaussian fitting of satellite peaks in Figure 5 for T40V40, T5V5, and T3V3 superlattices, respectively, the relationship $(M/\Gamma)^2 = I_2/I_1$, where $\Gamma = 375$ meV is the inverse core-hole lifetime estimated from photoemission, gives the values of $M = 198$, 180, and 172 meV, respectively, for the e -ph coupling energy.^[64] In terms of the often used dimensionless ratio $M/\hbar\omega_0$ the e -ph coupling has the values of 2.2, 2.1, and 1.9 respectively. These values are about a factor of two lower than that for bulk anatase with a coupling constant ≈ 5 ,^[64] and indicate that the e -ph coupling gradually becomes weaker with decreasing superlattice period. The weakening of the e -ph coupling and the smearing out of phonon harmonics could be caused by interfacial distortion of TiO_2 bonding that becomes more pronounced for short period superlattices for which the

number of interfaces increases inversely proportional to the period at a fixed film thickness.

2.3. Characterization of the Electronic Structure of VO_2 using XAS and RIXS

The XAS spectra of the V $L_{3,2}$ -edge and the O K -edge of VO_2 layers in the superlattices are illustrated in Figure 6. The V L_3 and V L_2 absorption peaks at 518 and 525 eV arise from V $2p_{3/2}$ to V $3d$ and V $2p_{1/2}$ to V $3d$ transitions, respectively. The O K -edge above the V L_2 edge that involves transitions from occupied O $1s$ to empty O $2p$ states is indicative of covalent mixing of O $2p$ -V $3d$ orbitals. The two peaks between 528 and 534 eV are attributed to O $2p$ -V $3d$ hybridized π^* and σ^* bands of the V $3d$ t_{2g} and e_g states formed by crystal field splitting.^[66] Other than a slight shift toward lower photon energies with increasing superlattice period, the V $L_{3,2}$ -edge XAS does not exhibit obviously distinguishing features that could provide clues about the superlattice properties just from qualitative examination of the spectra. Instead, a MO based picture that was proposed for interpretation of the experimental data in terms of orbital switching in the V $3d$ states must be relied on.^[67] In this picture the V d orbitals were redefined with respect to the V chain along the rutile c -axis according to the already discussed Goodenough MO model^[11] to discriminate between two types of orbitals; the $d_{||}$ -orbitals formed by strong overlap of the lowest energy $d_{x^2-y^2}$ V t_{2g} orbitals between neighboring V atoms forming a chain, and the π^* -orbitals that form between the two other V t_{2g} orbitals.^[11,21] The comparison of the XAS spectra of the VO_2 thin film and the superlattices shows that the spectra change with the superlattice period. The most notable changes occur in the O K -edge region. These changes are straightforward to interpret as the linear combination of contributions from the O K -edges of VO_2 and TiO_2 . The π^* and σ^* orbitals

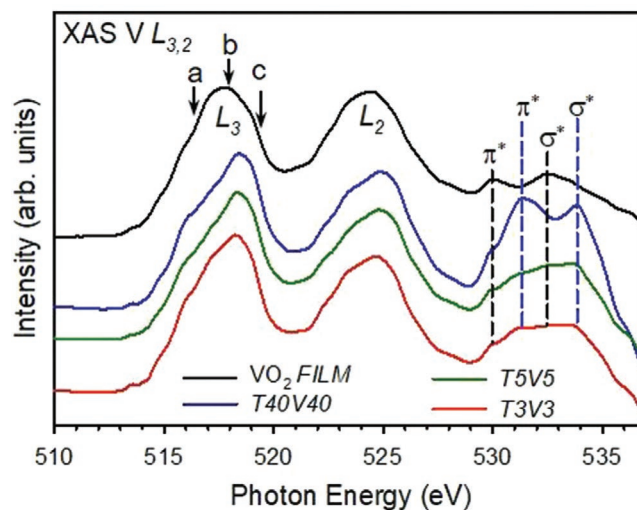


Figure 6. The V $L_{3,2}$ -edge and the O K -edge XAS spectra of the $(\text{TiO}_2)_m/(\text{VO}_2)_m$ superlattices as a function of superlattice period m , compared to a VO_2 film at 350 K. The spectra are vertically offset for clarity, and $a = 516.4$ eV, $b = 518$ eV, and $c = 519.4$ eV, designate the incident photon energies used for measuring the V L -edge RIXS spectra for π polarization.

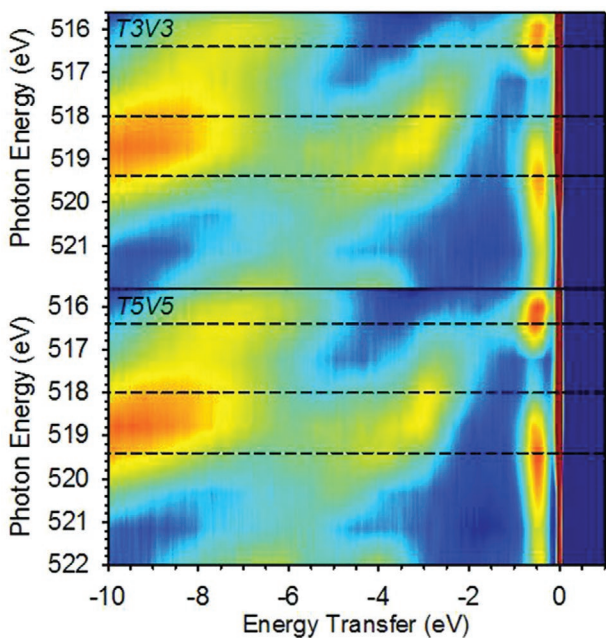


Figure 7. The intensity color maps for the $V L_3$ RIXS energy transfer as a function of the incident photon energy for $T3V3$ and $T5V5$ superlattices in the insulating state at 15 K. The dashed lines designate the discrete incident photon energies that were selected for measuring the RIXS spectra.

for the VO_2 film designated by black vertical dashed lines at 530 and 532.6 eV, and for the TiO_2 layers designated by blue vertical dashed lines at 531.4 and 533.8 eV, are in good agreement with literature values.^[66] With decreasing superlattice period these features smear out into one broad peak suggesting compositional intermixing in short period superlattices.

The MIT transition in VO_2 occurs by huge orbital switching accompanied by massive transfer of spectral weight.^[14,68,69] To illustrate the meaning of this picture for the superlattices we reiterate the key changes of the electronic structure resulting from orbital switching across the MIT in VO_2 . The best-known characteristic of the VO_2 MIT orbital picture is the splitting of the $d_{||}$ -band by V–V dimerization across the MIT that characterizes the M_1 insulating phase.^[11,21] In the metallic R phase the partially filled $d_{||}$ - and π^* -bands originating from t_{2g} orbitals overlap at the Fermi level. The hybridization of the apical V–O bonds increases in the insulating M_1 state. In addition, the π^* -band is shifted up in energy by the antiferroelectric distortion, so that only the $d_{||}$ -band below the Fermi level is occupied. The changes in the orbital occupation reduce the effective band width in the insulating state and the system becomes more 1D-like and susceptible to a Peierls transition that is coupled with massive orbital switching that can occur only in systems that are already close to a Mott insulating regime.^[67]

An overview of the spectral features of the L_3 V RIXS energy transfer as a function of the incident photon energy in a range between 515.6 and 522.0 eV is provided by the false color intensity maps in **Figure 7**. These two maps were selected as an example for comparing the energy loss signatures for a $T5V5$ superlattice with the MIT still intact, and a $T3V3$ superlattice with no longer observable MIT features in **Figure 2**. The two maps exhibit very similar color patterns, representing the

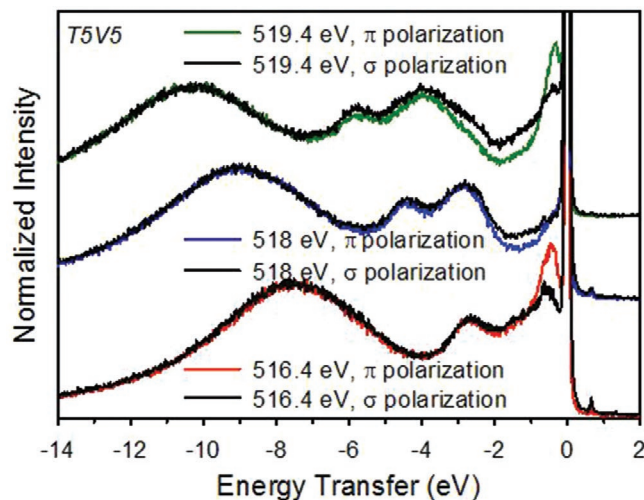


Figure 8. The polarization dependence of the RIXS spectra for three values of the incident photon energy in **Figure 6**, $a = 516.4$, $b = 518$, and $c = 519.4$ eV for the $T5V5$ superlattice at 350 K. The spectra were normalized by the intensity of the large CT peak and offset vertically for clarity.

spectral components and their respective weights, and reveal no obvious difference between the two superlattices in the insulating state. However, the energy loss spectra for discrete incident photon energies designated by dashed lines in **Figure 7** show important differences as a function of temperature and incident photon polarization. The three different incident photon energies illustrate the key signatures of the $V L_3$ -edge RIXS spectra in **Figure 8**. The RIXS spectrum for the 519.4 eV incident photon energy near the valley between the L_3 and the L_2 XAS peaks contains four peaks at 0.5, 4.0, 5.9, and 10.4 eV energy loss. The most important of these peaks is the Raman response in the dd excitation region at 0.5 eV. The intensity of this peak is also strongly polarization dependent and is maximized for π polarization with the electric field vector parallel to the rutile c -axis ($E||c$). According to the MO model it corresponds to transitions from the $d_{||}$ orbital to $e_g^\pi(\pi^*)$ orbital.^[70,71] The remaining three peaks in **Figure 8** are much broader than the dd transition and according to the energy maps show dispersion with the incident photon energy suggesting that they correspond to CT and fluorescence excitations.

The dd spectral region comparing several superlattices and the VO_2 film in the insulating state, in a temperature range of 15–80 K using incident photon energy of 519.4 eV, is illustrated in **Figure 9**. These spectra reveal several features that are not consistent with the presence of oxygen vacancies in the VO_2 layers. The most notable feature is that except the single peak at 0.5 eV corresponding to transitions within the t_{2g} subbands no other excitations are present. The absence of $V 3d^2$ RIXS spectral signature rules out the formation of V^{3+} indicating the absence of oxygen vacancies.^[57–60] It is important to note that the spectroscopic signature for the $d_{||}d_{||}^*$ transitions in the energy loss range between 1 and 2 eV is also absent in these spectra. The position of the 0.5 eV peak is clearly below 0.9 eV that was reported previously for this excitation.^[70] However, apart from the difference in resolution between the present study and that in Ref. [70] the differences in sample type can lead to changes in the crystal field splitting

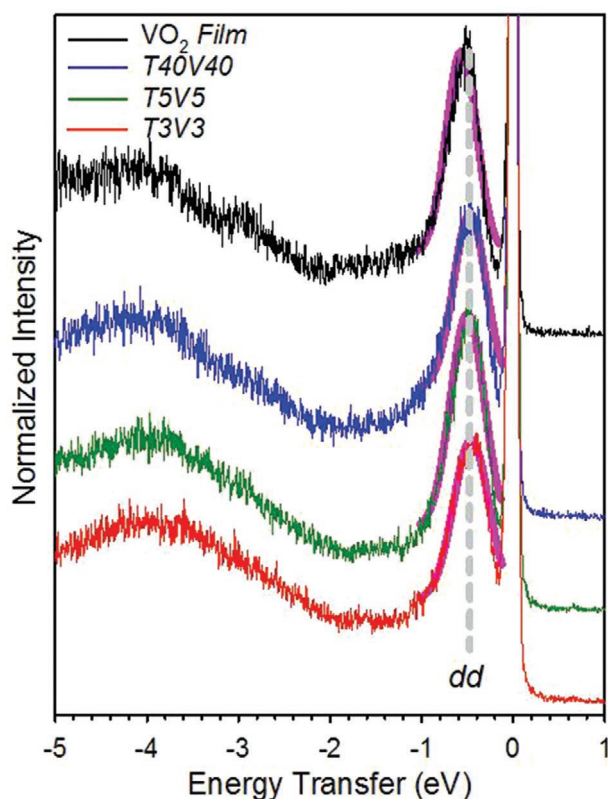


Figure 9. The width of the V $d_{||}$ RIXS peak in the insulating state in a temperature range of 15–80 K as a function of the superlattice period at incident photon energy of 519.4 eV. The magenta lines are Gaussian fits to the superlattices and the VO₂ film with FWHM of 240 ± 60 and 220 ± 60 meV, respectively. The spectra were normalized by the intensity of the large CT peak at 11 eV and offset vertically for clarity.

that can produce the observed shift in the energy loss of this excitation. Normalization to the maximum of the 11 eV energy loss CT band and Gaussian fitting of the peak profiles allows comparison of different superlattices based on the relative intensity of the dd peaks with respect to CT excitations. The peaks in Figure 9 show negligible energy shift. The FWHM

of 240 ± 60 meV does not change with superlattice period and within instrumental resolution is comparable to that for the VO₂ film of 220 ± 60 meV. The constant intensity of this peak that in the insulating state corresponds to the completely occupied $d_{||}$ orbital suggests that all electrons are tied up in the V–V dimers independent of the superlattice period.

Since it is already known from previous work that the orbital population in the insulating state is very robust and not affected by strain, it is not unexpected that oxygen vacancies would be difficult to form in the insulating state.^[21] In contrast, the metallic state was found to be more susceptible to oxygen vacancy formation.^[72] The RIXS spectra for the T5V5 superlattice in Figure 10 are similar to that for VO₂ thin films and are representative of the behavior of VO₂ across the MIT. The transition from the insulating to the metallic state in Figure 10 occurs by broadening of the 0.5 eV peak because the π^* orbitals shift down across the Fermi level as the π^* and $d_{||}$ orbitals become both partially occupied and overlap. It is intriguing that the T3V3 superlattice, which does not exhibit an MIT in Figure 2, shows qualitatively similar RIXS spectral features in this temperature range. However, neither the insulating nor the metallic phase in Figure 10 show any spectral features that could be attributed to V³⁺ and V $3d^2$ excitations.

3. Conclusions

The fabrication and characterization of the properties of (TiO₂)_m/(VO₂)_m superlattices with $m = 1, 3, 5, 20,$ and 40 has been undertaken as part of a general approach for using interfaces and superlattices for exploring novel concepts and phenomena in reduced dimensionality systems of strongly correlated oxides. The reason binary oxides are more versatile models for exploring strong correlation effects is that in contrast to perovskites that only share common corners of cation-occupied octahedra, binary-oxides can in addition share common edges and faces facilitating direct cation-to-cation interactions. The characterization of strain by XRD and temperature dependent transport measurements of the MIT reveal the existence of a new range of compositional and structural

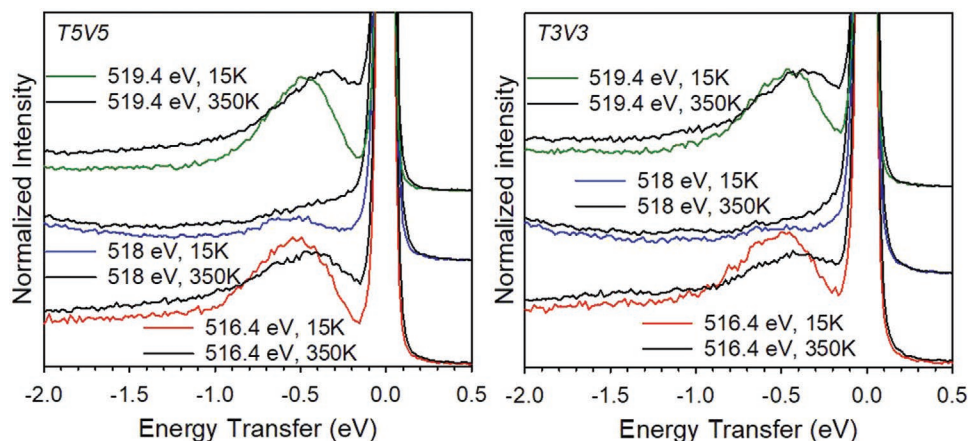


Figure 10. Comparison of the spectral weight transfer across the MIT for the T5V5 and the T3V3 superlattices, at three different incident photon energies and π polarization. The spectra were normalized by the intensity of the large CT peak and offset vertically for clarity.

metastability as a function of the superlattice period, m . The specific approach for tuning the electronic structure in VO_2 guided by X-ray spectroscopic measurements was inspired by recent experimental advances and theoretical predictions.^[21,30]

The significant new results of this work are related to the spectroscopic states revealing the delicate behavior of oxygen vacancies in both VO_2 and TiO_2 layers of the superlattices. The presence of oxygen vacancies in the metallization of VO_2 layers is considered to be established fact in the literature.^[43,44,48] In contrast, our X-ray spectroscopic data indicate that the dramatic changes in MIT can occur at unexpectedly low concentrations or even in absence of oxygen vacancies. Specifically, the RIXS spectra show no signature of V^{3+} states ruling out oxygen vacancy induced valence changes. The complete absence of oxygen vacancy related V^{3+} states is contradictory to the prevailing view that the MIT changes in the electrical transport data are induced by preferential accumulation of oxygen vacancies in VO_2 layers.^[43,44,48] The prevailing view is based on recent experimental data and theoretical calculations showing that oxygen vacancy formation is energetically favorable in the VO_2 layers^[43] creating a chemical potential difference that is a strong driving force for oxygen vacancy migration across the interface from the TiO_2 into the VO_2 layers.^[48] The presence of the weak Ti^{3+} peak of uncertain origin indicates that TiO_2 cannot be a major source of oxygen vacancies. Note that exposure to UV photons can create relative abundance of oxygen vacancies that could certainly explain the presence of dd excitations in the TiO_2 layers.^[73] Nevertheless, if beam induced transformation is a significant mechanism creating oxygen vacancies; their migration should still be prevalent, and detectable by the presence of V^{3+} related excitation in RIXS. Similarly, it was reported that no change of the V oxidation state was observed by XAS and photoemission spectroscopy, despite the distinctive features of oxygen vacancy driven MIT being clearly present in electrical transport data of samples grown at variable oxygen partial pressures.^[74] These results suggest that superlattice fabrication is capable of suppressing oxygen vacancy formation while still affording a wide tunability range of the MIT.

This work shows that superlattice fabrication introduces new tuning parameters in the binary oxide rutile phase space ideally suited for controlling the access to novel phenomena in reduced dimensionality systems of strongly correlated oxides. These phenomena are not materials specific and are likely to be widely applicable to other binary-oxide superlattices enabling the creation of novel metastable phases of matter simply by using the tuning parameters for precisely controlling superlattice periodicity described here.

4. Experimental Section

The $(\text{TiO}_2)_m/(\text{VO}_2)_m$ superlattices and the VO_2 thin film reference sample were grown by pulsed laser deposition (PLD) on (001) TiO_2 substrates. The VO_2 films and the VO_2 and TiO_2 superlattice layers were grown at an O_2 pressure of 10 and 15 mTorr, respectively, at a fluence of 1.2 J cm^{-2} , and 5 or 10 Hz repetition rate at $300 \text{ }^\circ\text{C}$ substrate temperature. The layer thickness was controlled by the number of laser shots required for the growth of monolayer that was calibrated separately for VO_2 and TiO_2 using X-ray reflectivity. For further details see Figure S1 and Supporting Information. After growth the samples were post annealed

in 100 mTorr of O_2 for 1 h and cooled down to room temperature at this pressure.

X-ray diffraction was performed by a four-circle high-resolution X-ray diffractometer (X'Pert Pro, PANalytical) using $\text{Cu-K}\alpha$ radiation. A standard four-point probe method was used to perform the electrical transport measurements of VO_2 films and $(\text{TiO}_2)_m/(\text{VO}_2)_m$ superlattices using a PPMS (Physical Property Measurement System, Quantum Design).

X-ray absorption and resonant inelastic X-ray scattering measurements were carried out at the ADRESS beamline of the Swiss Light Source at the Paul Scherrer Institut.^[75,76] All measurements were performed at grazing incidence with the X-rays incident at 15° with respect to the sample surface. The spectra were measured with linear polarization set either parallel (π) or perpendicular (σ) to the scattering plane. The scattering angle was fixed at 130° . The spectrometer was used in the high throughput configuration with the 1500 lines per mm variable line spacing spherical grating and the newly installed CCD camera that is capable of sub-pixel spatial resolution.^[77,78] The beamline exit slit was $20 \text{ }\mu\text{m}$. This setup yielded a full width at half maximum (FWHM) total energy resolution of around 60 meV.

Supporting Information

Supporting Information is available from the Wiley Online Library or from the author.

Acknowledgements

This research was sponsored by the U.S. Department of Energy (DOE), Office of Science, Basic Energy Sciences (BES), Materials Sciences and Engineering Division. This work was performed at the ADRESS beamline of the Swiss Light Source at the Paul Scherrer Institut (PSI). The work at PSI was supported by the Swiss National Science Foundation (SNSF) through the NCCR MARVEL and the Sinergia network Mott Physics Beyond the Heisenberg Model (MPBH) with SNSF grant numbers CRSII2_160765/1 and CRSII2_141962. X.L. acknowledges financial support from the European Community's Seventh Framework Programme (FP7/20072013) under Grant agreement No. 290605 (Cofund; PSI-Fellow). T.S. was supported by SNSF, Research Grant number 200021_178867, and M.R. by SNSF Research Grant 200021_182695.

Conflict of Interest

The authors declare no conflict of interest.

Keywords

binary oxide superlattices, metal insulator transitions, pulsed laser deposition, strongly correlated oxides, X-ray spectroscopy

Received: June 9, 2020

Revised: July 30, 2020

Published online: September 20, 2020

[1] F. J. Morin, *Phys. Rev. Lett.* **1959**, 3, 34.

[2] M. Imada, A. Fujimori, Y. Tokura, *Rev. Mod. Phys.* **1998**, 70, 1039.

[3] D. Lee, B. Chung, Y. Shi, G. Y. Kim, N. Campbell, F. Xue, K. Song, S. Y. Choi, J. P. Podkaminer, T. H. Kim, P. J. Ryan, J. W. Kim, T. R. Paudel, J. H. Kang, J. W. Spinuzzi, D. A. Tenne, E. Y. Tsymal, M. S. Rzchowski, L. Q. Chen, J. Lee, C. B. Eom, *Science* **2018**, 362, 1037.

- [4] M. Nakano, K. Shibuya, D. Okuyama, T. Hatano, S. Ono, M. Kawasaki, Y. Iwasa, Y. Tokura, *Nature* **2012**, *487*, 459.
- [5] Z. Yang, C. Ko, S. Ramanathan, *Annu. Rev. Mater. Res.* **2011**, *41*, 337.
- [6] M. Brahlek, L. Zhang, J. Lapano, H. T. Zhang, R. Engel-Herbert, N. Shukla, S. Datta, H. Paik, D. G. Schlom, *MRS Commun.* **2017**, *7*, 27.
- [7] J. del Valle, P. Salev, F. Tesler, N. M. Vargas, Y. Kalcheim, P. Wang, J. Trastoy, M. H. Lee, G. Kassabian, J. G. Ramirez, M. J. Rozenberg, I. K. Schuller, *Nature* **2019**, *569*, 388.
- [8] W. H. Brito, M. C. O. Aguiar, K. Haule, G. Kotliar, *Phys. Rev. Lett.* **2016**, *117*, 056402.
- [9] O. Nájera, M. Civelli, V. Dobrosavljević, M. J. Rozenberg, *Phys. Rev. B* **2018**, *97*, 045108.
- [10] T. M. Rice, H. Launois, J. P. Pouget, *Phys. Rev. Lett.* **1994**, *73*, 3042.
- [11] J. B. Goodenough, *J. Solid State Chem.* **1971**, *3*, 490.
- [12] N. F. Mott, L. Friedmann, *Philos. Mag.* **1974**, *30*, 389.
- [13] A. Liebsch, H. Ishida, G. Bihlmayer, *Phys. Rev. B* **2005**, *71*, 085109.
- [14] S. Biermann, A. Poteryaev, A. I. Lichtenstein, A. Georges, *Phys. Rev. Lett.* **2005**, *94*, 026404.
- [15] J. D. Budai, J. Hong, M. E. Manley, E. D. Specht, C. W. Li, J. Z. Tischler, D. L. Abernathy, A. H. Said, B. M. Leu, L. A. Boatner, R. J. McQueeney, O. Delaire, *Nature* **2014**, *515*, 535.
- [16] S. Wall, S. Yang, L. Vidas, M. Chollet, J. M. Glowina, M. Kozina, T. Katayama, T. Henighan, M. Jiang, T. A. Miller, D. A. Reis, L. A. Boatner, O. Delaire, M. Trigo, *Science* **2018**, *362*, 572.
- [17] J. Laverock, V. Jovic, A. A. Zakharov, Y. R. Niu, S. Kittiwatanakul, B. Westhenry, J. W. Lu, S. A. Wolf, K. E. Smith, *Phys. Rev. Lett.* **2018**, *121*, 256403.
- [18] N. F. Quackenbush, H. Paik, M. J. Wahila, S. Sallis, M. E. Holtz, X. Huang, A. Ganose, B. J. Morgan, D. O. Scanlon, Y. Gu, F. Xue, L. Q. Chen, G. E. Sterbinsky, C. Schlueter, T. L. Lee, J. C. Woicik, J. H. Guo, J. D. Brock, D. A. Muller, D. A. Arena, D. G. Schlom, L. F. J. Piper, *Phys. Rev. B* **2016**, *94*, 085105.
- [19] J. Laverock, S. Kittiwatanakul, A. Zakharov, Y. Niu, B. Chen, S. A. Wolf, J. W. Lu, K. E. Smith, *Phys. Rev. Lett.* **2014**, *113*, 216402.
- [20] D. Wegkamp, M. Herzog, L. Xian, M. Gatti, P. Cudazzo, C. L. McGahan, R. E. Marvel, R. F. Haglund, A. Rubio, M. Wolf, J. Stähler, *Phys. Rev. Lett.* **2014**, *113*, 216401.
- [21] N. B. Aetukuri, A. X. Gray, M. Drouard, M. Cossale, L. Gao, A. H. Reid, R. Kukreja, H. Ohldag, C. A. Jenkins, E. Arenholz, K. P. Roche, H. A. Dürr, M. G. Samant, S. S. P. Parkin, *Nat. Phys.* **2013**, *9*, 661.
- [22] V. Eyert, *Ann. der Phys.* **2002**, *11*, 650.
- [23] B. Lazarovits, K. Kim, K. Haule, G. Kotliar, *Phys. Rev. B* **2010**, *81*, 115117.
- [24] Z. Hiroi, *Prog. Solid State Chem.* **2015**, *43*, 47.
- [25] J. P. Pouget, H. Launois, J. P. D'Haenens, P. Merenda, T. M. Rice, *Phys. Rev. Lett.* **1975**, *35*, 873.
- [26] L. F. J. Piper, A. Demasi, S. W. Cho, A. R. H. Preston, J. Laverock, K. E. Smith, K. G. West, J. W. Lu, S. A. Wolf, *Phys. Rev. B* **2010**, *82*, 235103.
- [27] R. Ramesh, D. G. Schlom, *Nat. Rev. Mater.* **2019**, *4*, 257.
- [28] K. Shibuya, M. Kawasaki, Y. Tokura, *Phys. Rev. B* **2010**, *82*, 205118.
- [29] S. Ismail-Beigi, F. J. Walker, A. S. Disa, K. M. Rabe, C. H. Ahn, *Nat. Rev. Mater.* **2017**, *2*, 17060.
- [30] V. Pardo, W. E. Pickett, *Phys. Rev. Lett.* **2009**, *102*, 166803.
- [31] Z. Tang, F. Sun, B. Han, K. Yu, Z. Q. Zhu, J. H. Chu, *Phys. Rev. Lett.* **2013**, *111*, 107203.
- [32] J. L. Lado, D. Guterding, P. Barone, R. Valentí, V. Pardo, *Phys. Rev. B* **2016**, *94*, 235111.
- [33] K. Maekawa, M. Takizawa, H. Wadati, T. Yoshida, A. Fujimori, H. Kumigashira, M. Oshima, Y. Muraoka, Y. Nagao, Z. Hiroi, *Phys. Rev. B* **2007**, *76*, 115121.
- [34] S. Okamoto, A. J. Millis, *Nature* **2004**, *428*, 630.
- [35] J. K. Kawasaki, D. Baek, H. Paik, H. P. Nair, L. F. Kourkoutis, D. G. Schlom, K. M. Shen, *Phys. Rev. Mater.* **2018**, *2*, 054206.
- [36] J. B. Goodenough, *Phys. Rev.* **1960**, *117*, 1442.
- [37] J. B. Goodenough, *Prog. Solid State Chem.* **1971**, *5*, 145.
- [38] L. W. Martin, Y. H. Chu, R. Ramesh, *Mater. Sci. Eng. R Reports* **2010**, *68*, 89.
- [39] L. L. Fan, S. Chen, Z. L. Luo, Q. H. Liu, Y. F. Wu, L. Song, D. X. Ji, P. Wang, W. S. Chu, C. Gao, C. W. Zou, Z. Y. Wu, *Nano Lett.* **2014**, *14*, 4036.
- [40] V. Théry, A. Boulle, A. Crunteanu, J. C. Orlianges, *Appl. Phys. Lett.* **2017**, *111*, 251902.
- [41] Y. Muraoka, Z. Hiroi, *Appl. Phys. Lett.* **2002**, *80*, 583.
- [42] D. Marrocchelli, N. H. Perry, S. R. Bishop, *Phys. Chem. Chem. Phys.* **2015**, *17*, 10028.
- [43] J. Jeong, N. Aetukuri, T. Graf, T. D. Schladt, M. G. Samant, S. S. P. Parkin, *Science* **2013**, *339*, 1402.
- [44] D. Passarello, S. G. Altendorf, J. Jeong, M. G. Samant, S. S. P. Parkin, *Nano Lett.* **2016**, *16*, 5475.
- [45] N. F. Quackenbush, J. W. Tashman, J. A. Mundy, S. Sallis, H. Paik, R. Misra, J. A. Moyer, J. H. Guo, D. A. Fischer, J. C. Woicik, D. A. Muller, D. G. Schlom, L. F. J. Piper, *Nano Lett.* **2013**, *13*, 4857.
- [46] K. Nagashima, T. Yanagida, H. Tanaka, T. Kawai, *J. Appl. Phys.* **2007**, *101*, 026103.
- [47] R. D. Shannon, C. T. Prewitt, *Acta Crystallogr. Sect. B Struct. Crystallogr. Cryst. Chem.* **1969**, *25*, 925.
- [48] Y. Park, H. Sim, M. Jo, G. Y. Kim, D. Yoon, H. Han, Y. Kim, K. Song, D. Lee, S. -Y. Choi, J. Son, *Nat. Commun.* **2020**, *11*, 1401.
- [49] N. F. Quackenbush, H. Paik, M. E. Holtz, M. J. Wahila, J. A. Moyer, S. Barthel, T. O. Wehling, D. A. Arena, J. C. Woicik, D. A. Muller, D. G. Schlom, L. F. J. Piper, *Phys. Rev. B* **2017**, *96*, 081103.
- [50] E.-J. Guo, Y. Liu, C. Sohn, R. D. Desautels, A. Herklotz, Z. Liao, J. Nichols, J. W. Freeland, M. R. Fitzsimmons, H. N. Lee, *Adv. Mater.* **2018**, *30*, 1705904.
- [51] A. Kotani, S. Shin, *Rev. Mod. Phys.* **2001**, *73*, 203.
- [52] L. J. P. Ament, M. Van Veenendaal, T. P. Devereaux, J. P. Hill, J. Van Den Brink, *Rev. Mod. Phys.* **2011**, *83*, 705.
- [53] P. Krüger, *Phys. Rev. B* **2010**, *81*, 125121.
- [54] A. Augustsson, A. Henningsson, S. M. Butorin, H. Siegbahn, J. Nordgren, J. H. Guo, *J. Chem. Phys.* **2003**, *119*, 3983.
- [55] F. M. F. de Groot, J. C. Fuggle, B. T. Thole, G. A. Sawatzky, *Phys. Rev. B* **1990**, *41*, 928.
- [56] J. P. Crocombette, F. Jollet, *J. Phys.: Condens. Matter* **1994**, *6*, 10811.
- [57] T. Schmitt, L.-C. Duda, A. Augustsson, J.-H. Guo, J. Nordgren, J. E. Downes, C. McGuinness, K. E. Smith, G. Dhalenne, A. Revcolevschi, M. Klemm, S. Horn, *Surf. Rev. Lett.* **2002**, *9*, 1369.
- [58] M. Matsubara, T. Uozumi, A. Kotani, Y. Harada, S. Shin, *J. Phys. Soc. Japan* **2002**, *71*, 347.
- [59] D. E. McNally, X. Lu, J. Pellicciari, S. Beck, M. Dantz, M. Naamneh, T. Shang, M. Medarde, C. W. Schneider, V. N. Strocov, E. V. Pomjakushina, C. Ederer, M. Radovic, T. Schmitt, *npj Quantum Mater* **2019**, *4*, 6.
- [60] C. F. Hague, J. M. Mariot, V. Ilakovac, R. Delaunay, M. Marsi, M. Sacchi, J. P. Rueff, W. Felsch, *Phys. Rev. B* **2008**, *77*, 045132.
- [61] K. J. Zhou, M. Radovic, J. Schlappa, V. Strocov, R. Frison, J. Mesot, L. Patthey, T. Schmitt, *Phys. Rev. B* **2011**, *83*, 201402.
- [62] S. Butorin, J. Guo, M. Magnuson, J. Nordgren, *Phys. Rev. B* **1997**, *55*, 4242.
- [63] Y. Harada, M. Watanabe, R. Eguchi, Y. Ishiwata, M. Matsubara, A. Kotani, A. Yagishita, S. Shin, *J. Electron Spectros. Relat. Phenomena* **2001**, *114–116*, 969.
- [64] S. Moser, S. Fatale, P. Krüger, H. Berger, P. Bugnon, A. Magrez, H. Niwa, J. Miyawaki, Y. Harada, M. Grioni, *Phys. Rev. Lett.* **2015**, *115*, 096404.
- [65] L. J. P. Ament, M. Van Veenendaal, J. Van Den Brink, *EPL* **2011**, *95*, 27008.
- [66] M. Abbate, F. M. F. De Groot, J. C. Fuggle, Y. J. Ma, C. T. Chen, F. Sette, A. Fujimori, Y. Ueda, K. Kosuge, *Phys. Rev. B* **1991**, *43*, 7263.

- [67] M. W. Haverkort, Z. Hu, A. Tanaka, W. Reichelt, S. V. Streltsov, M. A. Korotin, V. I. Anisimov, H. H. Hsieh, H. J. Lin, C. T. Chen, D. I. Khomskii, L. H. Tjeng, *Phys. Rev. Lett.* **2005**, *95*, 196404.
- [68] T. C. Koethe, Z. Hu, M. W. Haverkort, C. Schüßler-Langeheine, F. Venturini, N. B. Brookes, O. Tjernberg, W. Reichelt, H. H. Hsieh, H. J. Lin, C. T. Chen, L. H. Tjeng, *Phys. Rev. Lett.* **2006**, *97*, 116402.
- [69] K. Okazaki, H. Wadati, A. Fujimori, M. Onoda, Y. Muraoka, Z. Hiroi, *Phys. Rev. B* **2004**, *69*, 165104.
- [70] L. Braicovich, G. Ghiringhelli, L. H. Tjeng, V. Bisogni, C. Dallera, A. Piazzalunga, W. Reichelt, N. B. Brookes, *Phys. Rev. B* **2007**, *76*, 125105.
- [71] H. He, A. X. Gray, P. Granitzka, J. W. Jeong, N. P. Aetukuri, R. Kukreja, L. Miao, S. A. Breitweiser, J. Wu, Y. B. Huang, P. Olalde-Velasco, J. Pelliciari, W. F. Schlotter, E. Arenholz, T. Schmitt, M. G. Samant, S. S. P. Parkin, H. A. Dürr, L. A. Wray, *Phys. Rev. B* **2016**, *94*, 161119.
- [72] S. Singh, T. A. Abtew, G. Horrocks, C. Kilcoyne, P. M. Marley, A. A. Stabile, S. Banerjee, P. Zhang, G. Sambandamurthy, *Phys. Rev. B* **2016**, *93*, 125132.
- [73] Z. Wang, Z. Zhong, S. McKeown Walker, Z. Ristic, J.-Z. Ma, F. Y. Bruno, S. Riccò, G. Sangiovanni, G. Eres, N. C. Plumb, L. Patthey, M. Shi, J. Mesot, F. Baumberger, M. Radovic, *Nano Lett.* **2017**, *17*, 2561.
- [74] S. Kittiwatanakul, J. Laverock, D. Newby, K. E. Smith, S. A. Wolf, J. Lu, *J. Appl. Phys.* **2013**, *114*, 053703.
- [75] V. N. Strocov, T. Schmitt, U. Flechsig, T. Schmidt, A. Imhof, Q. Chen, J. Raabe, R. Betemps, D. Zimoch, J. Krempasky, X. Wang, M. Grioni, A. Piazzalunga, L. Patthey, *J. Synchrotron Radiat.* **2010**, *17*, 631.
- [76] G. Ghiringhelli, A. Piazzalunga, C. Dallera, G. Trezzi, L. Braicovich, T. Schmitt, V. N. Strocov, R. Betemps, L. Patthey, X. Wang, M. Grioni, *Rev. Sci. Instrum.* **2006**, *77*, 113108.
- [77] T. Schmitt, V. N. Strocov, K. J. Zhou, J. Schlappa, C. Monney, U. Flechsig, L. Patthey, *J. Electron Spectros. Relat. Phenomena* **2013**, *188*, 38.
- [78] M. R. Soman, D. J. Hall, J. H. Tutt, N. J. Murray, A. D. Holland, T. Schmitt, J. Raabe, B. Schmitt, *Nucl. Instruments Methods Phys. Res. Sect. A Accel. Spectrometers, Detect. Assoc. Equip.* **2013**, *731*, 47.